PHYSICAL REVIEW B **72**, 064120 (2005)

Atomistic simulations of shock-induced transformations and their orientation dependence in bcc Fe single crystals

Kai Kadau,[1,*] Timothy C. Germann,[2,†] Peter S. Lomdahl,[1,‡] and Brad Lee Holian[1,§]
[1]*Theoretical Division, Los Alamos National Laboratory, Los Alamos, New Mexico 87545, USA*
[2]*Applied Physics Division, Los Alamos National Laboratory, Los Alamos, New Mexico 87545, USA*

(Received 25 March 2005; revised manuscript received 30 June 2005; published 25 August 2005)

By multimillion-atom classical molecular dynamics simulations employing an embedded atom method potential, we investigate shock-induced phase transformations in body-centered cubic Fe single crystals caused by shock loading along $[001]_{\mathrm{bcc}}$, $[011]_{\mathrm{bcc}}$, and $[111]_{\mathrm{bcc}}$ directions. Significant dependence of the developing microstructure on the crystallographic shock direction is evident, but we see only a weak dependence of the transition pressures for the body-centered→close-packed and solid→melt transitions on the shock direction. The Hugoniots obtained by simulations of samples with lengths approaching one micrometer are compared to experimental work for pressures and temperatures above shock-induced melting. Crystallographic relationships between the parent and product phase found in the simulations are common for martensitic transformations. We discuss the influence of different embedded atom method potentials on the dynamics of the transformation. We see solitary waves ahead of the shock front. The velocities of these waves decrease in time, such that they are absorbed into the shock front within a distance of propagation of one μm or less.

DOI: 10.1103/PhysRevB.72.064120 PACS number(s): 62.50.+p, 71.15.Pd, 81.30.Kf, 62.20.Fe

I. INTRODUCTION

Classical atomistic simulations on shock-induced plasticity in crystalline solids have a history of a quarter century.[1–16] Plasticity in a general sense can manifest itself in a variety of manners: dislocation generation, twinning, melting, structural phase transitions, chemical reactions, etc. The ultimate goal of such atomistic simulations is to understand the underlying physics at the atomistic level and thus be able to help guide and interpret experiments. However, one always has to carefully consider the limitations of atomistic simulations and their consequences when drawing conclusions. The three main problems of classical atomistic simulations are the limited length and time scales, as well as the assumptions made in the interatomic force law (including electronic contributions). All of those problems are coupled to computational time, and therefore simulations have greatly improved over the years. For instance, the theoretical length scale that can be simulated has now approached the μm scale[17] and interatomic force models have improved from simple hard-sphere systems[18] to (modified) embedded-atom method [(M)EAM] potentials for the description of metals and semiconductors.[19–22] However, it is noteworthy that general aspects of atomistic processes can be studied, even in systems having simple interactions like hard spheres or Lennard-Jones pair potentials.[1,2,4,6–9,14,16]

Iron has a ferromagnetic body-centered cubic (bcc) ground state (α-Fe), and hydrostatic compression experiments at room temperature show a transition to the nonmagnetic hexagonal close-packed (hcp) ϵ phase at 13 GPa, with the reverse transformation taking place at 8 GPa.[23] This hysteresis declines with increasing temperature and disappears at the triple point at about 800 K and 10.5 GPa. Here, the antiferromagnetic fcc γ-Fe phase appears. The shock-induced bcc to hcp transition in Fe was first discovered in 1956 by Bancroft *et al.*[24] at pressures[25] that are also around 13 GPa.[26–28] Upon unloading, a complete reversal of the transformation can occur. For Fe, as well as for other materials exhibiting structural phase transitions under shock loading, a split two-wave structure has been observed, where an elastic precursor is followed by the transformation wave.[26,27] Split two-wave structures have also been observed in atomistic simulations for dissociative transitions,[3] elastic-plastic behavior,[8] and for the polymorphic phase transformations in Fe.[13] In a previous paper,[13] we reported atomistic simulations of the shock-induced $\alpha \rightarrow \epsilon$ transition in iron single crystals shocked in the $[001]_{\mathrm{bcc}}$ direction. Here, we will extend that study to explore shock loading in other crystallographic directions, both for the $\alpha \rightarrow \epsilon$ and solid→melt transitions. Theoretical results will be compared to the available experimental data, to shed light on the dynamics and the underlying atomistic processes in such transformations, including the influence of the interatomic force model.

II. METHODS

We will focus on shock-induced transformations[13] in Fe as described by two different EAM potentials: a Voter-Chen (VC) potential[29] and the Meyer-Entel (ME) force-field.[30] Both potentials accurately reproduce the lattice constant, cohesive energy, elastic properties, and the vacancy energy of bcc Fe by their construction. In addition, the ME potential has been fit to zone-boundary phonon frequencies that are of particular importance when describing temperature-driven martensitic transformations from one solid phase to another.[31,32] However, under compression this potential is too stiff as compared to *ab initio* electronic structure calculations,[33] resulting in an unacceptably high shock-induced transition pressure of 55 GPa for shocks along the $[001]_{\mathrm{bcc}}$ direction (Fig. 1). The VC potential uses the empirical Rose equation of state[34] and compares well to electronic structure calculations of the ferromagnetic bcc ground state

1098-0121/2005/72(6)/064120(14)/$23.00

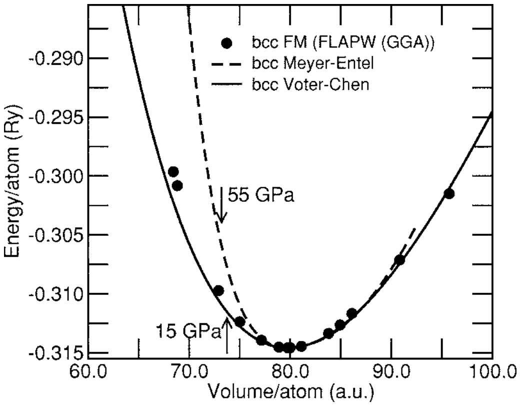

FIG. 1. Cold curve for the Meyer-Entel potential (dashed line) and the Voter-Chen potential (full line). The circles correspond to FLAPW (full potential augmented plane wave) with GGA (generalized gradient approximation) electronic structure calculations of the ferromagnetic bcc ground state of iron (the *ab initio* cold curve has been been shifted to the experimental ground state volume) (Ref. 33). Arrows indicate where the shock-induced transformation along the $[001]_{\mathrm{bcc}}$ direction occurs for each potential.

of iron, yielding a lower shock transition pressure of about 15 GPa.[13] The cold curve transition pressures (i.e., the intersection of the enthalpies $H=E+PV$ for two crystallographic structures) for the VC potential at $T=0$ are 9 and 13 GPa for the bcc → hcp and bcc → fcc transitions, respectively. More details of the VC potential are given in the Appendix.

Molecular dynamics (MD) simulations[35] were performed with both potentials, in order to compare their response to shock waves traveling through a perfect bcc crystal in the $[001]_{\mathrm{bcc}}$, $[011]_{\mathrm{bcc}}$, and $[111]_{\mathrm{bcc}}$ directions. However, most of the results presented here are based on the VC potential, except where the ME potential will be noted. While the quantitative results differ a lot for the two potentials, the qualitative nature of the phase transformation is very similar.

Nonequilibrium molecular dynamics (NEMD) simulations used the Scalable Parallel short-range molecular dynamics (SPaSM) code[17,36,37] with shock waves induced by slamming the sample up against a specularly reflecting wall at piston velocity u_p (the so-called momentum mirror method[4,38]). In NEMD no additional coupling of the atoms to a heat bath is done, since shock waves are assumed to be adiabatic (i.e., no heat exchange with the environment). Other approaches to the impact process have been tried, where the atoms are not reflected so perfectly in order to see whether the perfectly flat mirror produced artifacts. The initial lattice temperature of the samples was set either to 50, or 300 K to see if initial temperature matters. The sample sizes ranged from about $N=1$ million to 8 million atoms and the sample length in the shock direction from about 60 nm to 1 μm. The CPU-intensive calculations were performed on Los Alamos' QSC-machine[17] using up to 512 CPUs.[39]

Since the computational cost for NEMD simulations goes like Nt, where t is the time simulated, the cost of shock simulations by NEMD rises quadratically with the duration of the physical shock simulation time (a doubling of the system length is required for a doubling of the shock compression time). In uniaxial Hugoniostat MD simulations,[9] N is independent of the shock propagation time and can be much smaller than in NEMD. The uniaxial Hugoniostat modifies the classical Newtonian equations of motion, such that the system relaxes to a state on the Hugoniot (i.e., the locus of final shock states). Starting with a perfect crystal the simulation cell is uniaxially compressed instantaneously to its final value before the individual motions of the atoms are switched on. This leads to an infinite strain rate in the uniaxial Hugoniostat simulations as compared to a high but finite strain rate in shock experiments or NEMD simulations. Therefore, these simulations yield by their construction the correct Hugoniot for the system but have an upper limit on shock strength for their applicability to the dynamics of shock-induced plasticity and phase changes. We have run Hugoniostat simulations for up to 420 000 time steps (about 300 ps), which corresponds to a shock traveling almost 2 μm.

In the MD simulations presented here (containing N atoms in three dimensions) a coupled set of $3N$ second-order differential equations is solved numerically by the symplectic leapfrog algorithm.[35,40] The integration time step we used for the shock simulations varied from 0.73 to 1.46 fs for production runs, and was cut in half for some runs to check for convergence.

Analyzing the huge amount of data produced by such atomistic simulations is a daunting challenge, requiring special techniques. For example, in order to distinguish between bcc, uniaxially compressed bcc, grain boundaries, and the close-packed phase, we count the neighbors n for each atom within 2.75 Å (between the first and second peak of the bcc-Fe radial distribution):[13] bcc ($n=8$), uniaxially compressed bcc ($n=10$), grain boundaries ($n=11$), close-packed ($n=12$). We calculate the centrosymmetry parameter[41] for all atoms that are denoted as close-packed (by the neighbor counting). By setting the centrosymmetry threshold to $0.07a^2$ (the threshold for partial dislocations in a fcc lattice with lattice constant a) we can distinguish between fcc and hcp. We also calculated the time-dependent profiles of the particle velocity and other quantities like temperatures and pressure components (e.g., the pressure in the shock direction and the maximum shear pressure). After looking at the profiles, a suitable threshold can be determined, in order to identify the moving shock front and thus the shock velocity. A video (30.5 MB) of a typical run can be viewed here.[42]

III. RESULTS

A. bcc → hcp/fcc transition

The behavior previously reported[13] for VC Fe crystals shocked in the $[001]_{\mathrm{bcc}}$ direction remains qualitatively similar for the ME potential or for other loading directions. In particular, for low piston velocities a perfectly elastic shock front with an atomically sharp front is observed. Above a critical shock strength, within the uniaxially compressed bcc phase, small nuclei of the hcp/fcc phase start to first form, then grow on a picosecond time scale, leading to a second (transformation) shock front, which is not as atomically sharp as the leading elastic wave. At larger shock strengths, when the transformation wave catches up with the leading elastic wave, this split two-wave character vanishes. We observe an initial homogeneous nucleation of the hcp/fcc phase, followed by continuous growth of this phase, forming the transformation shock wave (for a shock strength right at the threshold for homogeneous nucleation, multiple nucleation sites have been observed). A similar mechanism has been identified for shock-induced plasticity in fcc crystals[14] under $[100]_{\mathrm{fcc}}$ compression, although $[111]_{\mathrm{fcc}}$ loading results in a "galloping" plastic wave, with new dislocations periodically nucleated.[16]

Although VC and ME potentials both exhibit essentially the same crystallographic structures, and split two-wave shocks in an intermediate shock strength regime, properties such as the quantitative Hugoniot are quite different: VC Fe transforms for shocks in $[001]_{\mathrm{bcc}}$ direction at pressures around 15 GPa into a close packed phase, and ME at about 55 GPa. There is a slight dependence of the VC Fe transition pressure with respect to the crystallographic shock direction: Whereas the $[001]_{\mathrm{bcc}}$ direction transforms at a longitudinal pressure of about 15 GPa, the $[011]_{\mathrm{bcc}}$ and $[111]_{\mathrm{bcc}}$ directions transform at somewhat higher pressures of about 18 and 20 GPa, respectively. A closer look reveals a large dependence of the evolving microstructure on the crystallographic shock direction (Fig. 2). For shocks in the $[001]_{\mathrm{bcc}}$ direction, the evolving grains consists mostly of the hcp structure with occasional stacking faults (i.e., local fcc) and are relatively large (Fig. 3). Here, two twinned variants of the product phase are observed that are separated by grain boundaries (noncoherent twin boundaries). Well below the melting transition, the evolving grains for shocks in the $[011]_{\mathrm{bcc}}$ and $[111]_{\mathrm{bcc}}$ directions are smaller and contain larger amounts of fcc (Fig. 4). In the latter cases, the variants contain hcp and fcc material and are slightly rotated relative to one another. As described above, the cold curve transition pressure of the VC Fe is higher for the bcc → fcc transition than for the bcc → hcp transition, which might explain the slightly different dynamic transition pressure for different shock directions. We should emphasize that within the EAM formalism the differences between fcc and hcp are not well described, so the relative amount of transformed hcp and fcc might not be reliable.

The observed transformations have martensitic character,[43,44] i.e., temperature-driven structural phase transformations that occur in a collective (shear/shuffle-like) manner, where the parent and product phases have specific crystallographic orientational relationships.[45] The transformation mechanism for shocks along $[001]_{\mathrm{bcc}}$ appears to be shuffle dominated, whereas the mechanism for shocks along $[011]_{\mathrm{bcc}}$ and $[111]_{\mathrm{bcc}}$ have large shear contributions (see the shape changes in Fig. 5). By looking at the neighborhood of the atoms before and after the transformation, we can see that the neighborhood is almost conserved after the transformation, with the most perfect conservation for shocks in the $[001]_{\mathrm{bcc}}$ direction. This means that the atoms do not have to move large distances in order to achieve the transformation; hence the observed transformation is prompt and occuring on a picosecond time scale (see Sec. III B). A closer look at the resulting crystallographic orientational relationships between the two phases reveal differences: for shocks in the $[001]_{\mathrm{bcc}}$ direction we observe $[001]_{\mathrm{bcc}} \| [\bar{1}\bar{1}20]_{\mathrm{hcp}}$ (hcp analog to $[1\bar{1}0]_{\mathrm{fcc}}$) and $(110)_{\mathrm{bcc}} \| (0001)_{\mathrm{hcp}}$ ($(111)_{\mathrm{fcc}}$ analog), and for shocks in the $[011]_{\mathrm{bcc}}$ direction $[011]_{\mathrm{bcc}} \| [0001]_{\mathrm{hcp}}$ ($[111]_{\mathrm{fcc}}$ analog) and $(100)_{\mathrm{bcc}} \| (\bar{1}\bar{1}20)_{\mathrm{hcp}}$ ($(1\bar{1}0)_{\mathrm{fcc}}$ analog). This is called the Nishiyama-Wassermann relation (or its hcp analog). However, in the case of shocks along $[011]_{\mathrm{bcc}}$ we observe minor deviations from the aforementioned relation, and also observe regions (with a much reduced occurrence) with a different transformation mechanism, where the $(011)_{\mathrm{bcc}}$ planes transform into $(001)_{\mathrm{fcc}}$. For shocks in the $[111]_{\mathrm{bcc}}$ direction we observe the Pitsch relation that is common for thin bcc Fe films deposited on a Cu $[001]_{\mathrm{fcc}}$ substrate:[46] $[111]_{\mathrm{bcc}} \| [110]_{\mathrm{fcc}}$ and $(1\bar{1}0)_{\mathrm{bcc}} \| (001)_{\mathrm{fcc}}$. Again, we observe minor deviations from this relationship in this shock direction. All of these relationships have been observed in Fe and its alloys and suggest that the transformation path can be described as a combination of the Bain transformation, shuffle-and-shear, and a rotation.[43]

The grain size of the transformed material in the overdriven region (but well below the melting transition) is much larger in the $[001]_{\mathrm{bcc}}$ shock direction than in $[011]_{\mathrm{bcc}}$ and $[111]_{\mathrm{bcc}}$ (Figs. 2–4). With increasing shock strength the grain size decreases,[13] and close to the shock melting transition it is similar for the three directions investigated. In the $[011]_{\mathrm{bcc}}$ and $[111]_{\mathrm{bcc}}$ orientations, the grain size is much less dependent on the shock strength than in the $[001]_{\mathrm{bcc}}$ direction. The radial distribution function of the transformed material reveals that the structural difference at a moderate shock strength ($u_p = 1087\ \mathrm{m/s}$) is much more strongly dependent on the crystallographic shock direction than for a shock closer to the melting transition ($u_p = 2174\ \mathrm{m/s}$) (Fig. 6).

In all directions the grain size directly at the shock front is smallest and increases on the nanometer length scale to larger, energetically more favorable grains. However, especially for shocks in the $[011]_{\mathrm{bcc}}$ and $[111]_{\mathrm{bcc}}$ directions we cannot exclude further relaxation that may take place on much longer time and distance scales than are accessible to our simulations. The different dynamics for the three different crystallographic shock directions are also reflected in the longitudinal pressure profiles (Fig. 7), particularly in the relaxation of the shear stress. Hayes observed experimentally different time scales (depending on the crystallographic shock direction) for the dynamics of shock-induced phase transformations in KCl single crystals,[47] and Knudson and Gupta for CdS crystals.[48]

In our simulations, we observe oscillatory signals in all three directions near the shock front. For particular shock strength regions (depending on the shock direction) these oscillations can move out ahead of the shock front. In Sec. III E we will discuss this in detail for the $[111]_{\mathrm{bcc}}$ direction. These oscillatory waves have already been observed in other atomistic simulations for fcc crystals.[6,8]

Shocks directed along the $[001]_{\mathrm{bcc}}$ direction can show an over-relaxation of the shear stress (i.e., a shear state of opposite sign, where the lateral stress is larger than the longitudinal stress in the shock direction) for shock strengths not

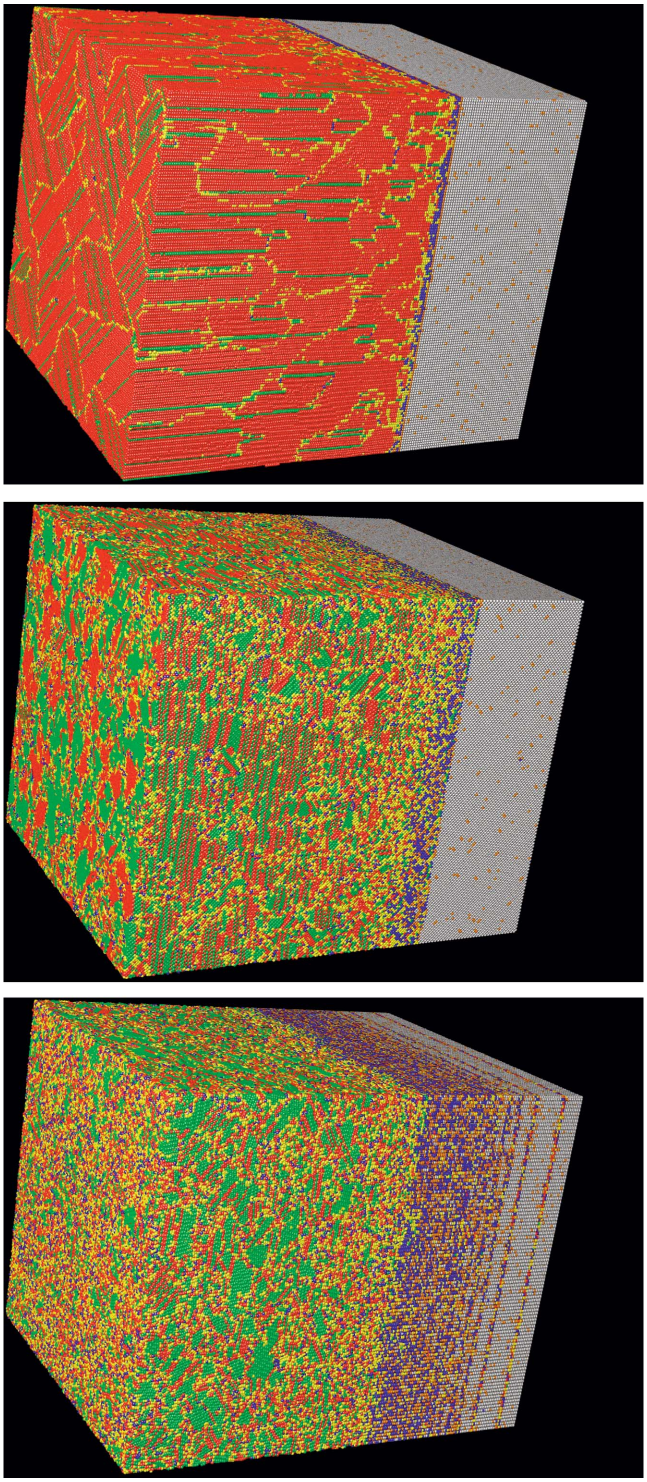

FIG. 2. (Color) Shocked samples (with $u_p = 1087$ m/s) containing approximately 8 million atoms (≈ 40 nm $\times$ 40 nm $\times$ 57 nm) after 6.57 ps. The shock front moved from left to right for shocks in $[001]_{\mathrm{bcc}}$, $[011]_{\mathrm{bcc}}$, and $[111]_{\mathrm{bcc}}$ directions (top to bottom). Color coding was obtained by counting neighbors (n) in combination with the centrosymmetry parameter (see the text for details): gray: bcc ($n=8$), blue: uniaxially compressed bcc ($n=10$), yellow: grain boundaries ($n=11$), red: hcp ($n \geqslant 12$, no centrosymmetry), green: fcc ($n \geqslant 12$, centrosymmetry). The region near the piston (left) was removed so that bulk rather than surface properties can be seen at the left side of the samples.

too far above the transformation threshold. This is due to the transformation mechanism in this particular shock direction: The ideal $(001)_{\mathrm{bcc}}$ plane distance is about 10% larger than the $(110)_{\mathrm{fcc}}$ plane distance into which the $(001)_{\mathrm{bcc}}$ planes are transforming, which can result in an overshoot for not too high shock strengths.[49] However, in time this overshoot is partly reduced by creating a mixed phase region (i.e., back-transforming close-packed material into bcc).

For shocks along $[001]_{\mathrm{bcc}}$, upon reflection at the free surface, the transformation is almost ideally reversible for shock strengths that are not too large (for example, $u_p = 1.45$ km/s). In this case the release wave has two parts: a nonshock release that is faster than the backtransformation wave that steepens to a shock front. This mechanism was suggested by Zel'dovich and Razer,[50] as well as by Hayes[51] in the case of polymorphic materials. For a higher shock strength (for example, $u_p = 2.18$ km/s), no backtransformation was observed on the time scales accessible and therefore no release shock wave was present. For even higher shock strength, but still lower than the shock-induced melting strength, a melting transition on the release was observed. However, we have not systematically investigated the release behavior, nor spallation.

B. Nucleation for different EAM potentials

The initial homogeneous nucleation as observed for shocks in the $[001]_{\mathrm{bcc}}$ direction can be described as a lateral movement of groups of atoms (Fig. 8). These initial nucleation sites are activated by thermal fluctuations, grow in time until different sites touch each other, and different variants evolve, separated by grain boundaries. The transformation front is created on a picosecond time scale. The growth of the initial nucleii is faster in the $[110]_{\mathrm{bcc}}$ and $[1\bar{1}0]_{\mathrm{bcc}}$ planes than perpendicular to these planes, which makes the initial nucleii more flat than round. A simple theory for homogeneous nucleation of martensites[43] assumes the nucleus to be a thin oblate spheroid. The Gibbs free-energy gain of a nucleus is due to the Gibbs free-energy gain of the volume of the new phase. This is opposed by the interface energy of the nucleus with the embedding parent phase and the elastic strain energy. The minimization of the two latter contributions to the Gibbs free energy determines the form of the nucleus: if the elastic strain energy is dominant, the shape is flat such that the elastic energy is minimized. On the other hand, if the interface energy is more important, the shape is more spherical to minimize the interface energy. This can be nicely seen in the simulations using the ME potential that should have a large elastic strain contribution due to its stiffness: the nucleii are flat (Fig. 8). The much softer VC potential exhibits rounder nucleii, demonstrating the lesser importance of the elastic strain energy with respect to the interface energy. With increasing shock strength, the number of homogeneous nucleation sites increases and the process is even more prompt. Eventually for high shock strengths, the initial nucleation process is virtually instantaneous with the shock front, and cannot be observed.

We should emphasize that the transformation shock front develops on a picosecond time scale in the present case of

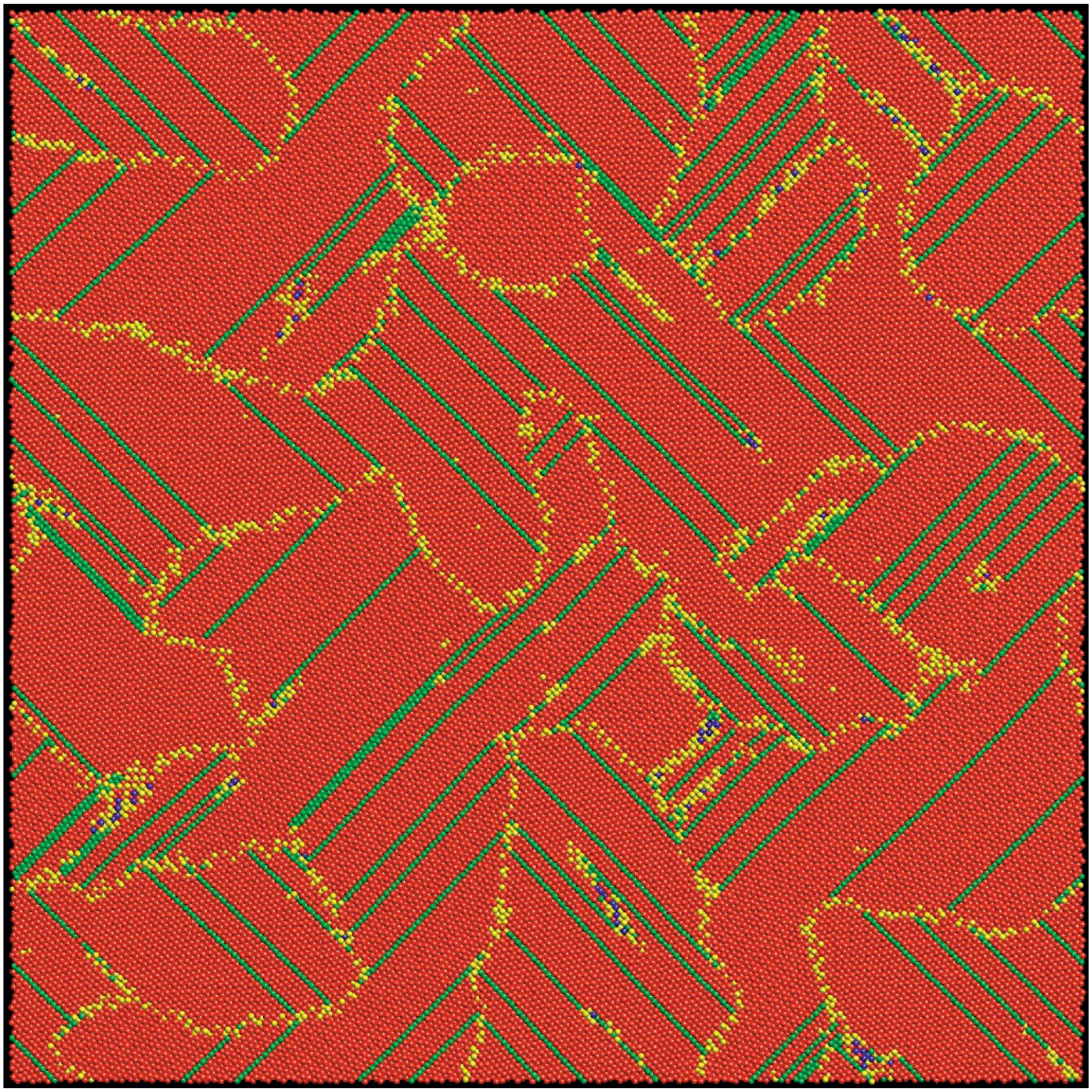

FIG. 3. (Color) Cross section of the sample shocked along the $[001]_{\mathrm{bcc}}$ direction shown in Fig. 2: two twinned variants of the product phase can be identified by looking at the diagonal green lines (local fcc, stacking faults in the red hcp structure). It can be seen that the yellow grain boundaries indeed separate regions with different crystallographic orientation. Color coding as in Fig. 2.

homogeneous nucleation, i.e., when the Gibbs free-energy barrier between the bcc and the hcp/fcc state can be overcome by thermal fluctuations. By introducing defects, the transformation threshold can be lowered, which we have seen in preliminary simulations that include defects. The threshold is lowered by locally reducing the Gibbs free-energy barrier, which makes it possible for the new phase to nucleate at defects. This means defects can lower the threshold down to the pressure where the Gibbs free energy of the two phases are equal. Between the lower thermodynamic equilibrium pressure of the bcc and the hcp/fcc phases and the higher pressure where homogeneous nucleation takes place, it might take much longer to build the transformation shock front. For shocks along $[001]_{\mathrm{bcc}}$, this region can be estimated to be bracketed by the cold curve transition pressure of 9 GPa and the dynamic transition pressure of 15 GPa. It could be expected that in the presence of defects, the dynamic transition pressure can be reduced to about 9 GPa—too low compared to experiments. In this region the typical time scale for the shock-induced transformation should depend on the defect density and the pressure above the threshold. Gas gun experiments on polycrystalline Fe samples show a different time scale for the $\alpha \rightarrow \epsilon$ transformation[51,52] for shocks with pressures of 16.5 and 14.5 GPa.

C. Hugoniot

In order to measure a steady wave velocity with good statistics, we have found that the sample length should be 0.5 μm, corresponding to about 60 ps simulation time (Fig. 9). The shock front velocity u_s is obtained by following the drop in the particle velocity profile (Fig. 10). Transformation waves in the two-wave region and oscillatory fronts are more difficult to analyze. In these cases long systems help to average out statistical fluctuations. In order to exclude any ar-

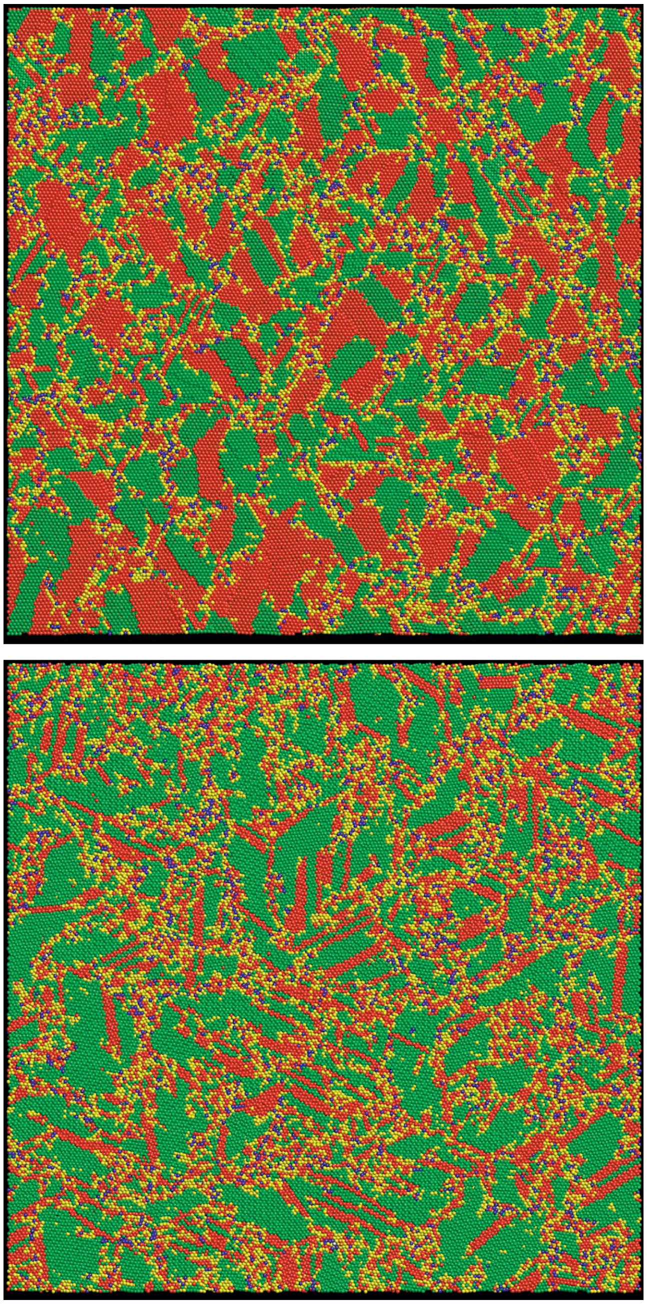

FIG. 4. (Color) Cross-sections of the samples shocked along the $[011]_{\mathrm{bcc}}$ (top) and $[111]_{\mathrm{bcc}}$ (bottom) directions shown in Fig. 2: smaller grains are formed and the amount of fcc atoms (green) is increased as compared to shocks along $[001]_{\mathrm{bcc}}$. Color coding as in Fig. 2.

tifacts that might be associated with the perfectly flat momentum mirror we use for generating the shocks, we did some runs where the shocks were generated by a symmetric impact of two equivalent pieces of material. No difference in the shock wave propagation was observed. The only difference observed is a higher temperature ($\approx 20\%$ for intermediate shock strength) in the vicinity of the momentum mirror. These differences vanish about 10 lattice constants away from the impact plane.

For piston velocities below the melt transition, the front velocities overshoot at the beginning and relax to a lower steady value. The higher the shock strength, the faster the relaxation process (10–30 ps; see the four largest shock velocities in Fig. 10), while for shocks exceeding the melt transition point the front velocity is observed to be steady from the beginning (on a sub-10 ps time scale; not shown in Fig. 10). However, for low shock strengths we cannot observe a relaxation to lower front velocities, which could be due to the limited simulation time (see the smallest shock velocities in Fig. 10).

Figure 11 shows the Hugoniots obtained by NEMD simulations and uniaxial Hugoniostat MD for single crystals together with experimental polycrystalline data.[28] The initial velocity of the solitary waves we observe for shocks in $[111]_{\mathrm{bcc}}$ are also shown (see Sec. III E). The experimental data has only points for the overdriven region and therefore no comparison for the low shock strength region can be done. The overdriven region compares well in general with the experimental data. However, the slope of the shock velocity as a function of the piston velocity is somewhat larger for the experiments, suggesting that the VC potential is a little too soft upon compression, as is suggested by the comparison of the cold curve for the Voter-Chen potential and *ab-initio* electronic structure calculations (Fig. 1).

Although the elastic part[53] and the split two-wave region of the Hugoniot exhibit similar features for all three directions, they differ quantitatively. For large shock strength they converge for all investigated directions. However, the convergence is not complete at the point where all directions are overdriven as one might expect, which has to do with a different microstructure (including a different size of evolving grains of the close packed material). Another interesting feature, especially pronounced for shocks in the $[001]_{\mathrm{bcc}}$ directions, is the convexity of the Hugoniot above the overdriven region: as described above, the front velocities seem to overshoot and then relax to a lower value in time. However, right above the overdriven regime these time scales do not seem to be accessible to our simulations, or this mechanism does not exist in this regime. In a certain regime uniaxial Hugoniostat simulations for up to 300 ps (corresponding to shock traveling about 2 μm) yield a lower shock velocity than the NEMD (see Fig. 11, inset). There the lower shock velocity is due to a somewhat different microstructure for the uniaxial Hugoniostat simulations. It is still an open question whether the convexity of the Hugoniot would vanish for simulations of much longer samples. Especially for shocks in the $[001]_{\mathrm{bcc}}$ direction the grain size is relatively large in this regime, which makes it stiffer than the other two shock directions with their smaller grains. This might explain the aforementioned convexity of the Hugoniot for $[001]_{\mathrm{bcc}}$ shocks: the decreasing grain size with shock strength makes the material softer,[54] thereby bending the Hugoniot toward lower shock velocities. In general, the uniaxial Hugoniostat simulations compare well with the NEMD simulations. However, the constant-volume uniaxial Hugoniostat simulations have an infinite strain rate, which can overshoot into a different microstructure or the melt phase (see below), where the system becomes dynamically trapped. In this case, it is better to employ the newly developed constant-stress Hugoniostat,

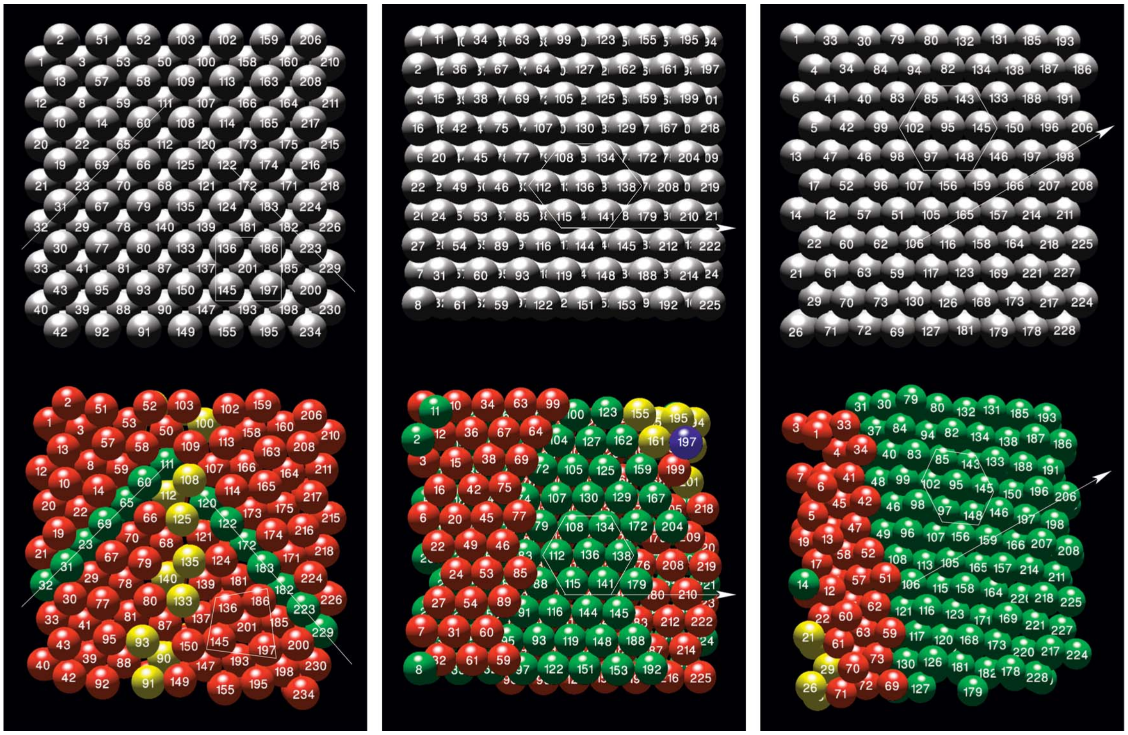

FIG. 5. (Color) Close-ups of the cross sections before (bcc, top) and after the transformation (hcp/fcc, bottom) for shocks in the $[001]_{bcc}$ (left), $[011]_{bcc}$ (middle), and $[111]_{bcc}$ (right) directions ($u_p = 1087$ m/s). The shock moves perpendicularly into the page. The neighborhood of the atoms is almost conserved during the transformation, as can be seen by the numbers on each atom. For example ($[001]_{hcp}$ shock direction, left), atom 201 has 136, 186, 197, and 145 as neighbors in both phases. The $[001]_{bcc}$ shock direction (left) transforms into the $[\bar{1}\bar{1}20]_{hcp}$ and $(110)_{bcc} \| (0001)_{hcp}$ (as defined by white lines and the direction perpendicular to the page). The $[011]_{bcc}$ shock direction (middle) transforms into the $[0001]_{hcp}$ ($[111]_{fcc}$) (typical distorted hexagons and hexagons of these planes are marked), with $[100]_{bcc} \| [\bar{1}\bar{1}20]_{hcp}([\ 1\bar{1}0)_{fcc}])$ (as marked by the arrows). The $[111]_{bcc}$ shock direction (right) transforms into $[110]_{fcc})$ with $[1\bar{1}0]_{bcc} \| [001]_{fcc}$ (as marked by the white arrows). The same atoms are shown in the parent (bcc) and the product (hcp/fcc) phase in order to demonstrate the shear ($[011]_{bcc}, [111]_{bcc}$)/shuffle ($[001]_{bcc}$) character of the transformation (color coding as in Fig. 2).

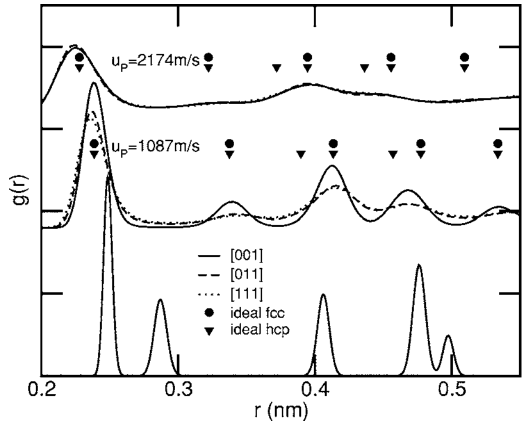

FIG. 6. Radial distribution functions of the transformed material for crystals shocked in different directions with a piston velocity $u_p = 2174$ m/s (top) and $u_p = 1087$ m/s (middle). As a reference the ideal positions of the fcc and the hcp structures, as well as the distribution function for the unshocked bcc, are shown (bottom). The radial distribution is less dependent on the shock direction for larger shock strengths, where a highly defective hcp/fcc product is generated regardless of orientation.

with a piston that is controlled by a parameter related to a finite rate of strain.[55]

We do not observe bcc plasticity before the phase transformation threshold, which would lead to a three-wave structure. Presumably the Hugoniot elastic limit for the perfect bcc crystal in our simulations is higher than the phase transformation threshold. However, starting right before the onset of shock-induced transformation in the $[001]_{bcc}$ shock direction, we observe a very tiny splitting of the elastic wave that seems to be connected to some enhancement of lateral movement of the atoms. We attribute this to a subcritical homogeneous nucleation process whereby the material begins to transform into the close-packed phase but does not have enough fluctuations to overcome the Gibbs free-energy barrier.[32] This picture is consistent with our observation that imperfect crystals have a lower transformation threshold than the perfect crystal simulations presented here. We also observed that these nucleation attempts can be successful, and the new phase develops and grows slowly, both in the direction of the shock propagation and the opposite direction. Here, a mixed phase in the form of stripes is observed, where the time scales to build a steady transformation wave exceed our simulation time scales (on the order of 60 ps). This means that close to the threshold for the transformation, the transformations are not so prompt. This might be particularly

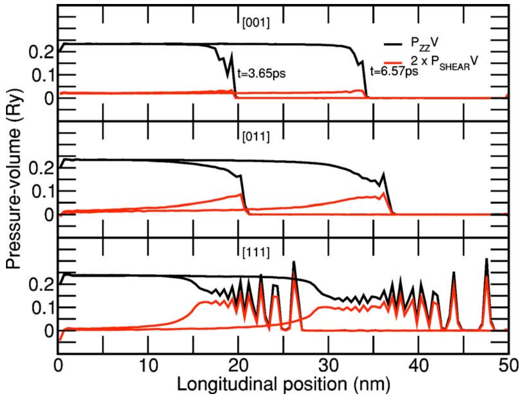

FIG. 7. (Color online) Profiles of the components of the pressure-volume tensor ($P_{ij}V, i,j=x,y,z$): longitudinal ($P_{zz}V$) and twice the shear ($[P_{zz}-(P_{xx}+P_{yy})/2]V$). The shock waves ($u_p = 1087$ m/s) propagate from left to right. Profiles are shown for two different times for the three major cubic crystallographic orientations.

true for real (defective) materials, where this threshold is lowered and nucleation takes place in a heterogeneous manner at preexisting defects.

The influence of the temperature on the shock-induced transformation was investigated by running a series of simulations for shocks in the $[001]_{\mathrm{bcc}}$ direction with a starting temperature of 300 K instead of 50 K. As can be seen in the inset of Fig. 11, the Hugoniot (including the transformation pressure) does not depend very much on the initial temperature. The Hugoniot in the elastic region is a little softer, as compared to the samples with an initial temperature of only 50 K. The main reason for this is that the virial part of the pressure components, i.e., the force part that comes from the compression, is much larger than the kinetic part.

D. Melting transition

We investigated the shock-induced melting in Fe single crystals by NEMD and Hugoniostat MD. It was found that the melting pressure varies by less than 10 GPa with the crystallographic shock direction (Fig. 12). This is in contrast

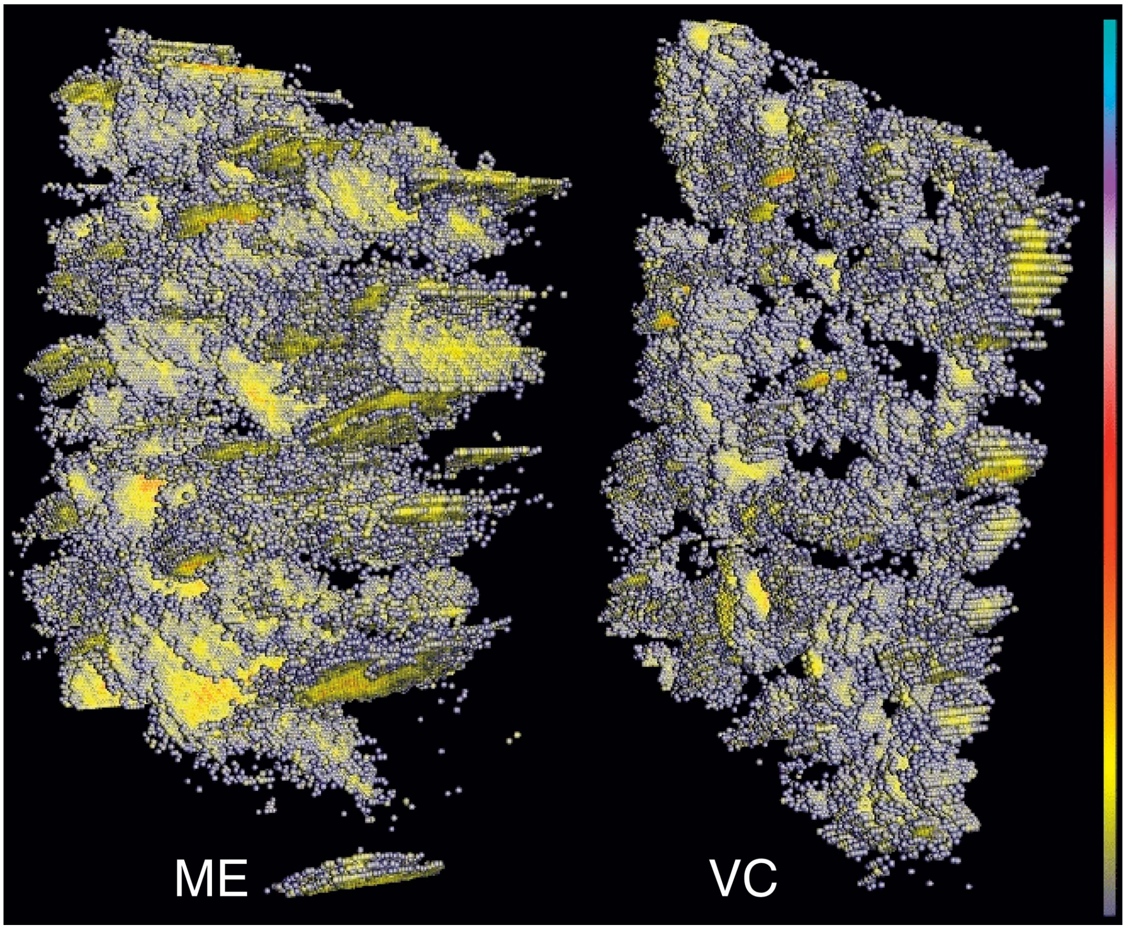

FIG. 8. (Color) Initial nucleation sites of close-packed iron within the uniaxially compressed bcc matrix at an early stage of nucleation for the Meyer-Entel potential (left: after 2.19 ps) and the Voter-Chen potential (right: after 1.095 ps). The shock strength for each potential is chosen to be just above the transformation threshold, i.e., $u_p=869.5$ m/s and $u_p=471$ m/s for the Meyer-Entel and the Voter-Chen potential, respectively. Only atoms with a transverse movement above 0.42 Å are shown, colored by their transverse displacement (gray $=0.42$ Å, cyan $\geqslant 1.32$ Å, about half the nearest neighbor distance). The nucleation sites for the Meyer-Entel potential appear to be more laminar than those for the softer Voter-Chen potential.

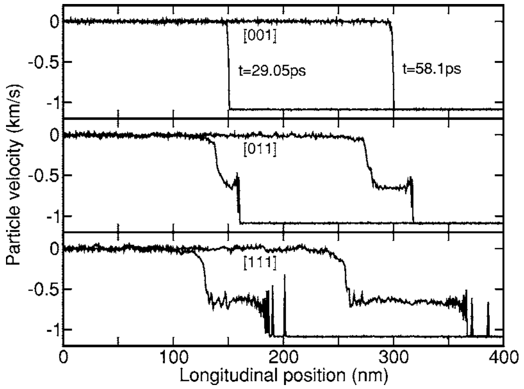

FIG. 9. Particle velocity profiles for shocks in different crystallographic orientations as obtained from NEMD for piston velocities $u_p = 1087$ m/s. The shock front velocity u_s can be obtained by following the drop in the particle velocity; this applies also for split two-wave structures as shown here for $[011]_{\mathrm{bcc}}$ and $[111]_{\mathrm{bcc}}$ directed shocks. The piston (longitudinal position=0) is at rest in the reference frame, which means the shock velocity is the measured front velocity in the reference frame plus the piston velocity.

to a large dependence (>50 GPa) in Cu single crystal simulations.[56] A dynamic argument for the orientational independence in the polymorphic metal Fe is that the original bcc lattice is unstable close to the shock-induced melting, which makes it easier to homogeneously nucleate melting (as compared to fcc Cu single crystals, which are stable even under large compression). The shock-induced microstructural grain size and radial distribution (Fig. 6) right below melting in the case of Fe is not very dependent on the shock direction, indicating that there is probably not much memory of the initial bcc crystal shock direction. Therefore, the shock-induced melting is not strongly dependent on the shock direction (Fig. 12).

For shock strengths close to melting, we observe an overshoot into the melt for uniaxial Hugoniostat simulations. Here, one has to run the simulations long enough (for about 50 ps) to give the system time to relax back into a solid phase. However, for some simulations close to the shock-induced melting point the system does not find its way back to the solid structure but rather gets stuck in a metastable supercooled liquid structure. This results in a slightly lower temperature than the solid phase in the P-T Hugoniot plot (see, for example the cross in the inset of Fig. 12 at 210 GPa). For the same initial compression one can observe both scenarios, demonstrating that the supercooled liquid just does not find a path to the solid structure in the given time. The closer the shock strength is to the observed melting point the longer it takes the system to go back to the solid phase, once it overshoots into the liquid. In the NEMD simulations we also observe this phenomena, however, it occurs in a narrower region of shock strength, reflecting the fact that the strain rate in the uniaxial Hugoniostat simulations is infinite but finite in NEMD simulations. Here, one can observe that within the melted material a solid nucleus starts to grow, both in the direction of the shock and opposite to it. Since the material overshoots into the melt and does not have enough time to relax back into the solid phase, the observed melting point is too low. For both the uniaxial Hugoniostat and the NEMD simulations, we only took the averages of pressure and temperature in the solid or the liquid region, depending on which was dominant (as shown in Fig. 12). Thus, there are no data points in the two-phase region between the liquid and the solid Hugoniot.

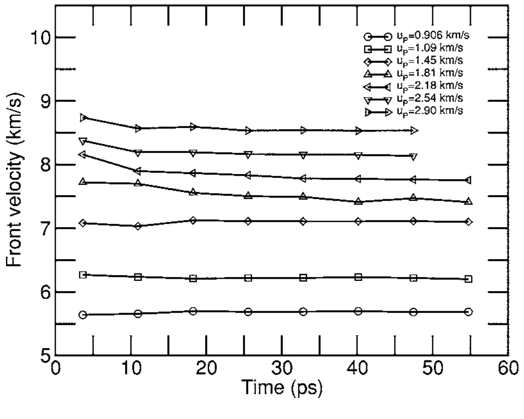

FIG. 10. Development of the front velocity for shocks in $[001]_{\mathrm{bcc}}$ direction for different piston velocities u_p. The shock velocity was determined to be the average of the last half of the simulations where the front velocity does not change very much. The sample length is close to $\approx 0.5\ \mu$m.

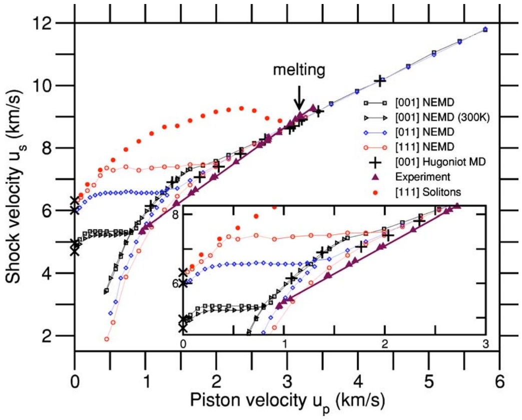

FIG. 11. (Color online) Single crystal Hugoniots for different crystallographic shock orientations as obtained by NEMD and uniaxial Hugoniostat simulations, compared to experimental polycrystalline data (Ref. 28). The crosses indicate the sound speed at zero temperature of the potential for the bulk (4695 m/s) and the $[001]_{\mathrm{bcc}}$ (4958 m/s), $[011]_{\mathrm{bcc}}$ (6004 m/s), and $[001]_{\mathrm{bcc}}$ (6315 m/s) directions (bottom to top). The arrow marks shock-induced melting, as obtained in the simulations. The solid circles mark the initial velocity of the solitons appearing for shocks in the $[111]_{\mathrm{bcc}}$ direction.

The temperature drop at the shock-induced melting reflects the latent heat of the material and is also observed in experiments;[57] however, the melting point is lower in the simulations than in experiments.[57,58] The VC Fe has a lower shock-induced melting temperature than real Fe. The calculated melting temperature at zero pressure of the VC Fe is 1470 K, compared to 1800 K in experiments. Note that VC Fe is a little softer than electronic structure calculations predict (Fig. 1).

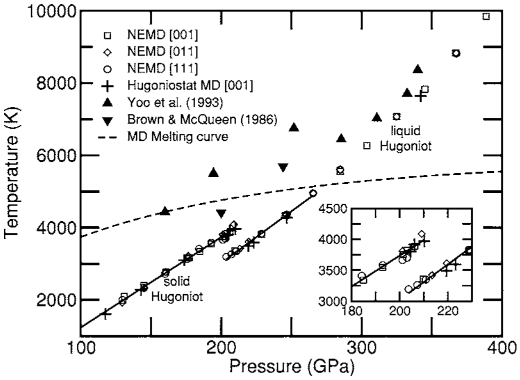

FIG. 12. P-T Hugoniots obtained from simulations (starting temperature 50 and 0 K for NEMD and Hugoniostat simulations, respectively) near the shock-induced melting transition as compared to experimental results (starting temperature 300 K). The experimental data points from Brown and McQueen represent shock anomaly points that are attributed to a hcp/fcc (left point) and the fcc/liquid phase transformation. Not much orientation dependence on the melting temperature is observed for these Fe single crystals. The equilibrium melting curve between perfect fcc and the melt (dashed line) as obtained by two-phase NVE MD simulations lies above the shock-induced melting. This might be attributed to the fact that the shock probes the melting between a highly defective crystal and the melt.

There is still some controversy in the experimental literature[57–61] regarding both the shock-induced and static high pressure melting of iron. For example, it is an open question where the hydrostatic melting curve lies with respect to shock-induced melting. Since experimentally it is difficult to achieve pressures of more than 100 GPa in hydrostatic experiments, the comparisons with the shock-induced melting is done by extrapolating the hydrostatic melting curve from low pressures to high pressures, which usually gives good agreement. In the MD simulations we found the melting line (perfect fcc/melt)[62] to be somewhat above the shock-induced melting, partly due to the overshooting in our NEMD and Hugoniostat simulations. The shock probes the melting line between the melt and a highly defected solid state, whereas the thermodynamic melting line describes the melting of a perfect crystal. Highly defective solids, like the shocked state before melting, are expected to have a lower melting point than perfect crystals. The thermodynamic melting point of massively defective solids is an open question. However, these kinetic effects are more pronounced in the MD simulations presented here since the time scales are far less than in macroscopic experiments. Yoo *et al.*[57] show that the shock-induced melting can be somewhat lower than the extrapolated hydrostatic melting curve (see Fig. 2 in Ref. 57).

Shock experiments suggest a pressure-induced hcp→fcc ($\epsilon \rightarrow \gamma$) phase transformation at a pressure of 200 GPa, before shock-induced melting at 243 GPa.[58] By extrapolating electronic structure calculations[33] we found the fcc phase energetically favored over the hcp phase at high pressures, which is also true for the VC Fe. The most stable solid structure near the shock-induced melt transition is probably fcc. Therefore we compared our shock-induced melting data with the fcc melting curve. Even if the hcp melting curve is slightly below the fcc melting line, the experimental melting curve is for the most stable solid structure.[63]

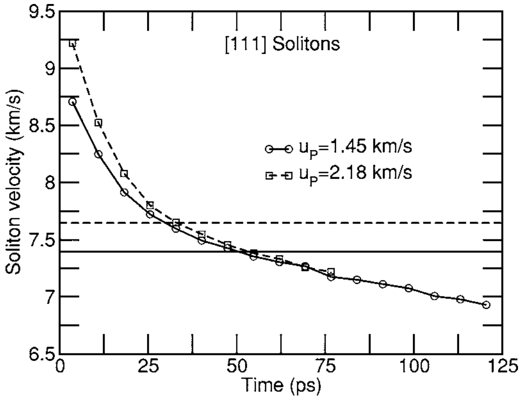

FIG. 13. Decay of the velocity of the first solitary wave for two different shock strengths in the $[111]_{\mathrm{bcc}}$ direction. Eventually the soliton velocity drops below that of the shock front (solid and dashed line for $u_p = 1.45$ km/s and $u_p = 2.18$ km/s, respectively).

E. Solitary waves

We found solitary waves at the shock front in quantities like the particle velocity (e.g., Fig. 9), pressure components, and the longitudinal temperature (not apparent in the lateral temperature component, indicating a 1D effect). Depending on the crystallographic direction and the shock strength, we found that these solitary waves can be faster than the shock front and have similarities with solitons: they are relatively stable (no dispersion) and there is almost no interaction between solitons (we probed that by looking at the interaction between a forward-marching solitary wave and a backward-marching one that had been reflected from the free surface). To further distinguish between the solitary waves that are attached to the shock front and those that leave the front, we will call the latter solitons. For example, we found strong solitons at high shock strengths in the $[001]_{\mathrm{bcc}}$ direction and weak solitons in a small intermediate shock strength regime for shocks along $[011]_{\mathrm{bcc}}$. Most pronounced are solitons in the $[111]_{\mathrm{bcc}}$ direction, and the discussion in this section is concentrated on this orientation (two solitons are visible as locally compressed regions in front of the shock front in Fig. 2, bottom). The $[111]_{\mathrm{bcc}}$ direction is a very stiff direction as is $[011]_{\mathrm{fcc}}$, where such solitons also have been observed.[8] Solitons are also found in shocked granular matter, where contact forces are dominant. Solitons have been studied for example in the one-dimensional Toda lattice.[64] Experiments in linear chains of steel beads[65] and MD simulations of steel beads[66] have also exhibited solitons.

However, the solitons we observe are nonideal, since they decay in time (Fig. 13). They have a dissipative interaction with the environment that slows them down, so that the trailing shock front eventually catches up with them on a micrometer length scale (Fig. 14). The decay of their velocity v does not obey a simple friction law with a friction coefficient C of the form $\dot{v} = -Cv^n$, $n = 1, 2, 3, \ldots$ ($n = 1$: Stokes friction,

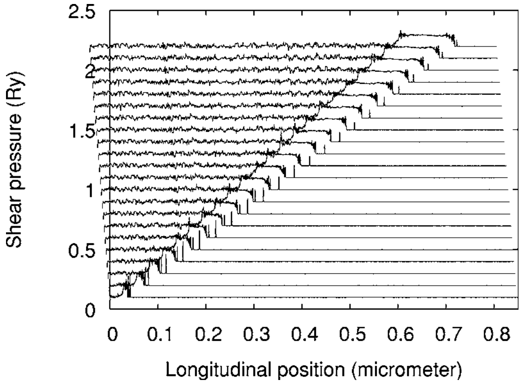

FIG. 14. Position-time plot of the evolution (every 5.84 ps) of the shear stress profile ($[111]_{\mathrm{bcc}}, u_{u_p}=1.45$ km/s, $T=50$ K). The decay of the peak height of the leading solitary wave is visible. The second emitted soliton gets caught about halfway up in the time evolution, while the leading soliton almost gets caught by the elastic precursor shock front at the end.

$n=2$: Newton friction), underlining their complex nature.

Another interesting feature is that these shock wave solitons only exist within a certain range of shock strengths; for overdriven shocks the initial soliton velocity no longer increases with shock strength, and by melting are not visible at all (Fig. 11). As the initial lattice temperature increases, the solitons become rarer. The latter observation together with the fact that solitons get caught by the shock front on the micrometer scale will make them challenging to observe experimentally.

The solitons result from the process of shock generation itself. They are produced once at the beginning and not continuously during the propagation (Fig. 14). However, in order to see whether they are an artifact of the perfectly flat momentum mirror, we did simulations with a symmetric impact, as well as other methods that add additional noise to the shock generation process. These methods did not seem to alter the behavior of the solitons very much. Even by employing a mirror in which the atoms are reflected by a fixed slab of atoms with an incommensurate (below the periodicity length) surface with respect to the shocked structure, the qualitative nature of the solitons was conserved. Roth[67] observed a dependence of the solitons as a function of the deviation angle of the ideal shock direction: Solitons vanish to within some degree of inclination, but come back at a lower intensity with an even larger angle of inclination.

IV. CONCLUSIONS

We have discussed in detail the dynamics of solid-solid and solid-liquid shock-induced transformations in bcc Fe single crystals by means of large-scale NEMD and uniaxial Hugoniostat MD. The sample length in the shock direction was up to 1 μm in NEMD, while Hugoniostat MD was performed for up to 300 ps (corresponding to a shock traveling about 2 μm). For the two different EAM potentials studied, the qualitative nature on the shock response does not differ much, e.g., they both exhibit a split two-wave structure in the intermediate shock strength regime and have the same crystallographic orientational relationships between the parent and product phases. A quantitative comparison with experimental data requires the correct equation of state. The VC Fe has a cold curve transition pressure that is about 4 GPa too low as compared to experiments and electronic structure calculations.[33] The dynamic transition pressure as observed in NEMD with perfect single crystals is about 6 GPa larger than the cold curve transition pressure. Within this regime, heterogeneous nucleation at defects is dominant, so that defects lower the dynamic transition pressure. Future work should also include different types of potentials that can better capture the complexity of iron. For instance, it was not possible to fit EAM potentials in the form of the ME potential to additional *ab initio* data in a reasonable way, since the flexibility of the formalism is limited. The more general modified embedded-atom method (MEAM)[21] might be suited to be parametrized by electronic structure calculations and experiments to describe Fe more reliably. Effects that are coupled to the magnetism of Fe are completely absent from the framework of (M)EAM and, therefore, other theoretical methods are needed to complement the findings presented here.

The quantitative comparison of our MD data with polycrystalline experimental data is satisfying, though not perfect, since the pressure range from 0 to over 300 GPa is greatly beyond that over which the potential was fit. Our simulations show that the shock-induced transformations (solid-solid and solid-liquid) are prompt for strong shocks where homogeneous nucleation is dominant (picosecond scale in single crystals). The solid-solid transformation is a martensitic-like transformation with atoms preserving their neighbor atoms; parent and product phases have a fixed crystallographic orientational relationship that is well known in martensitic transformations. We observed relaxation processes that exceeded 150 ps (or a sample length of one micrometer) and depend on the crystallographic shock direction. These features could be verified with modern small scale *in situ* x-ray diffraction experiments. The early detailed and forthcoming comparisons of small-scale experiments done at the OMEGA laser in Rochester on 200 μm single crystalline Fe films show good agreement with our atomistic simulations in terms of the transformation mechanism and the microstructure of the product phase.[68] These experiments, and additional small-scale extended x-ray absorption fine structure (EXAFS) of laser-induced (OMEGA) shocks in 8 μm thick polycrystalline Fe reveal that the shock-induced transformation is prompt and takes place on a subnanosecond time scale.[69] The latter polycrystalline experiments show a temperature increase from 300 to 645 K and a volume compression of 1.2 for shocks at $\approx$36 GPa, very similar to our theoretical single crystal results (565 K, 1.22, 37 GPa).

The shock-induced melting was found to be almost independent of the crystallographic shock direction. Shock-induced melting occurred at temperatures below the thermodynamic melting line of a perfect fcc crystal, suggesting that the melting curve under shock compression is that of a defective solid. Such thermodynamic and kinetic effects, including refreezing of a transient shock-induced supercooled liquid phase, deserves further study in comparisons of dynamic (shock Hugoniot) and static melting curves. Solitonlike waves produced at the impact plane move out ahead of the shock wave, but decay and get caught by the shock front on the micrometer scale. They are prominent in $[111]_{\mathrm{bcc}}$ shocks, but are suppressed by elevated temperatures.

Preliminary simulations of polycrystalline Fe show that the threshold of the shock-induced structural transformation is lowered relative to that of perfect single crystals. In polycrystals, nucleation takes place at the grain boundaries between nanograins of different orientation. Since defects are always present in real metals, more effort should be put into studying effects of defects.

The suggested mechanism of shock-induced phase transformations presented in this paper could be verified experimentally, since the time and distance scales for the atomistic simulations shown here are reaching the experimental micrometer scale.[68,69] The findings and methods presented in this paper can be used as a prototype to explore much more complex polymorphic materials like Ga (Ref. 22), Sn (Ref. 70), and Pu and their response to shock loading.

ACKNOWLEDGMENTS

We would like to thank D. J. Funk (Los Alamos), H. C. Herper (Duisburg), D. H. Kalantar (Livermore), E. M. Kober (Los Alamos), R. J. Ravelo (Texas), B. A. Remington (Livermore), J. Roth (Stuttgart), A. Strachan (Los Alamos), J. S. Wark (Oxford), B. Yaakobi (Rochester), and S. V. Zybin (Caltech) for many fruitful discussions. This work has been supported by the U.S. Department of Energy under Contract No. W-7405-ENG-36, with funding by ASC, and LDRD-DR 20020053 *Probing the Structural Dynamics of Condensed Matter using Ultrafast X-ray Diffraction*. QSC computer access through the Institutional Computing Program is gratefully acknowledged.

APPENDIX: EAM VOTER-CHEN FE POTENTIAL

Within the EAM formalism the potential energy E of a system containing N equal atoms can be written as a sum of the embedding energy F and a pair potential ϕ:

$$E = \sum_{i}^{N} F(\rho_i) + \sum_{i<j}^{N} \phi(r_{ij}), \tag{A1}$$

where r_{ij} is the distance between atoms i and j. The function $F(\rho_i)$ represents the embedding energy of atom i depending on the background electronic density,

$$\rho_i = \sum_{i\neq j}^{N} \rho_j^{\mathrm{at}}(r_{ij}). \tag{A2}$$

TABLE I. Properties of the VC and ME potentials compared to experimental data (taken from Refs. 29 and 30). Asterisks denote quantities constrained in the fitting procedure.

	Experimental	VC	ME
bcc lattice constant (Å)	2.870	2.870^{*}	2.870^{*}
Elastic constants (10^{12} dyn/cm^2)			
C_{11}	2.432	1.93	2.51
C_{12}	1.381	1.63	1.304
C_{44}	1.219	1.05	1.187
Bulk modulus	1.73	1.73^{*}	1.71
Vacancy energy (eV)			
relaxed	2.0	1.64	
unrelaxed		1.93	1.5

The Voter-Chen (VC) Fe potential uses a Morse pair potential,

$$\phi(r) = \nu_1(1 - e^{-\nu_3(r-\nu_2)})^2 - \nu_1, \tag{A3}$$

with $\nu_1 = 0.046\,46$ Ry, $\nu_2 = 2.092$ Å, and $\nu_3 = 1.343$ Å^{-1}. The atomic electronic densities are taken as

$$\rho^{\mathrm{at}}(r) = r^6(e^{-\nu_4 r} + 512 e^{-2\nu_4 r}), \tag{A4}$$

with $\nu_4 = 6.262$ Å^{-1}. The cutoff distance for the pair potential and the atomic electronic densities was set to 4.524 Å (between the third and fourth shell for the Fe bcc and fcc structures) and the functions were adjusted for smoothness at the cutoff. The embedding function F is determined such that the cohesive energy of bcc Fe satisfies the universal Rose equation of state.[34]

The VC potential describes the elastic properties of bcc Fe well (see Table I), the equation of state compares well to electronic structure calculations (Fig. 1), and the cold curve transition pressures for the bcc→hcp (fcc) is 9 GPa (13 GPa), which compares to 11.5 GPa for bcc→hcp, as obtained by electronic structure calculations.[33] These favorable characteristics led to our choice of this potential to describe the shock-induced $\alpha \rightarrow \epsilon$ in the framework of semiempirical descriptions. We calculated the thermodynamic melting temperature of the VC potential to be 1470 K, which is too low compared to the experimental 1800 K. This lower melting temperature is consistent with a lattice instability measured within the Parinello-Rahman scheme at around 1750 K for this potential.[28]

The VC potential does not reproduce accurately the temperature induced bcc→fcc.[29] Here, the ME potential has been shown to work,[32] although its equation of state is too stiff to describe the shock-induced transformation in a quantitative way. A more recent set of EAM Fe potentials[71] have been fit to various combinations of solid and liquid properties, and the more accurate description of the melting temperature, latent heat, and volume change, which should be useful for melt studies. This emphasizes the fact that simple semiempirical methods like the EAM are not suited to reliably describe all aspects of an element like Fe, but rather one has to either choose a description depending on the questions asked.

*Electronic address: kkadau@lanl.gov
†Electronic address: tcg@lanl.gov
‡Electronic address: pxl@lanl.gov
§Electronic address: blh@lanl.gov

[1] B. L. Holian and G. K. Straub, Phys. Rev. Lett. **43**, 1598 (1979).
[2] B. L. Holian, Phys. Rev. A **37**, 2562 (1988).
[3] D. H. Robertson, D. W. Brenner, and C. T. White, Phys. Rev. Lett. **67**, 3132 (1991).
[4] B. L. Holian and P. S. Lomdahl, Science **280**, 2085 (1998).
[5] J. D. Kress, S. R. Bickham, L. A. Collins, B. L. Holian, and S. Goedecker, Phys. Rev. Lett. **83**, 3896 (1999).
[6] V. V. Zhakhovskii, S. V. Zybin, K. Nishihara, and S. I. Anisimov, Phys. Rev. Lett. **83**, 1175 (1999).
[7] J. P. Hirth, R. G. Hoagland, B. L. Holian, and T. C. Germann, Acta Mater. **47**, 2409 (1999).
[8] T. C. Germann, B. L. Holian, P. S. Lomdahl, and R. Ravelo, Phys. Rev. Lett. **84**, 5351 (2000).
[9] J. B. Maillet, M. Mareschal, L. Soulard, R. Ravelo, P. S. Lomdahl, T. C. Germann, and B. L. Holian, Phys. Rev. E **63**, 016121 (2001).
[10] A. Strachan, T. Cagin, and W. A. Goddard, Phys. Rev. B **63**, 060103(R) (2001).
[11] S. V. Zybin, M. L. Elert, and C. T. White, Phys. Rev. B **66**, 220102(R) (2002).
[12] J. Roth, AIP Conf. Proc. **620**, 378 (2002).
[13] K. Kadau, T. C. Germann, P. S. Lomdahl, and B. L. Holian, Science **296**, 1681 (2002).
[14] D. Tanguy, M. Mareschal, P. S. Lomdahl, T. C. Germann, B. L. Holian, and R. Ravelo, Phys. Rev. B **68**, 144111 (2003).
[15] E. M. Bringa, J. U. Cazamias, P. Erhart, J. Stölken, N. Tanushev, B. D. Wirth, R. E. Rudd, and M. J. Caturla, J. Appl. Phys. **96**, 3793 (2004).
[16] T. C. Germann, D. Tanguy, B. L. Holian, P. S. Lomdahl, M. Mareschal, and R. Ravelo, Metall. Mater. Trans. A **35**, 2609 (2004).
[17] K. Kadau, T. C. Germann, and P. S. Lomdahl, Int. J. Mod. Phys. C **15**, 193 (2004).
[18] B. J. Alder and T. E. Wainwright, J. Chem. Phys. **27**, 1208 (1957).
[19] M. S. Daw and M. I. Baskes, Phys. Rev. Lett. **50**, 1285 (1983).
[20] M. S. Daw and M. I. Baskes, Phys. Rev. B **29**, 6443 (1984).
[21] M. I. Baskes, Phys. Rev. B **46**, 2727 (1992).
[22] M. I. Baskes, S. P. Chen, and F. J. Cherne, Phys. Rev. B **66**, 104107 (2002).
[23] E. F. Wassermann, M. Acet, P. Entel, and W. Pepperhoff, Phys. Status Solidi **82**, 2911 (1999).
[24] D. Bancroft, E. L. Peterson, and S. Minshall, J. Appl. Phys. **27**, 291 (1956).
[25] For shock experiments the transition pressure is the pressure component P_{zz} in the shock propagation direction.
[26] T. J. Ahrens, in *High-Pressure Shock Compression of Solids*, edited by J. R. Asay and M. Shahinpoor (Springer-Verlag, New York, 1993), Chap. 4, pp. 75–113.
[27] M. A. Meyers, *Dynamic Behavior of Materials* (Wiley-Interscience, New York, 1994).
[28] J. M. Brown, J. N. Fritz, and R. S. Hixson, J. Appl. Phys. **88**, 5495 (2000).
[29] R. Harrison, A. F. Voter, and S.-P. Chen, in *Atomistic Simulation of Materials*, edited by V. Vitek and D. J. Srolovitz (Plenum, New York, 1989), p. 219.
[30] R. Meyer and P. Entel, Phys. Rev. B **57**, 5140 (1998).
[31] P. Entel, R. Meyer, and K. Kadau, Philos. Mag. B **80**, 183 (2000).
[32] K. Kadau, P. Entel, T. C. Germann, P. S. Lomdahl, and B. L. Holian, J. Phys. IV **11**, 17 (2001).
[33] H. C. Herper, E. Hoffmann, and P. Entel, Phys. Rev. B **60**, 3839 (1999).
[34] J. H. Rose, J. R. Smith, F. Guinea, and J. Ferrante, Phys. Rev. B **29**, 2963 (1984).
[35] D. C. Rapaport, *The Art of Molecular Dynamics Simulation* (Cambridge University Press, Cambridge, 1995).
[36] P. S. Lomdahl, P. Tamayo, N. G. Jensen, and D. M. Beazley, in *Proceedings of Supercomputing '93*, edited by G. S. Ansell, IEEE Computer Society Press, 1993, p. 520.
[37] D. M. Beazley and P. S. Lomdahl, Comput. Phys. **11**, 230 (1997).
[38] The momentum mirror is at rest in the reference frame, which means that the moving shock front in the reference frame moves with the shock velocity u_s subtracted by the piston velocity u_p.
[39] Most of the samples were run on 64 CPUs within an 8 h run limit. Each 8 million atom sample shown in Fig. 2 was run on 6 processors of a SUN Server machine for about 6 days.
[40] The various flavors of Verlet integration algorithms are all second-order symplectic methods. Symplectic algorithms are favored due to their accurate conservation of the systems energy. Nonsymplectic methods that are higher order can solve chaotic many-body trajectories more accurately for a while, but over the long term exhibit a gradual increase in energy.
[41] C. L. Kelchner, S. J. Plimpton, and J. C. Hamilton, Phys. Rev. B **58**, 11085 (1998).
[42] See EPAPS Document No. E-PRBMDO-72-080530 for an MPEG movie of a strong shock moving through a bcc sample. This document can be reached via a direct link in the online article's HTML reference section or via the EPAPS homepage (http://www.aip.org/pubservs/epaps.html).
[43] L. Delaey, in *Phase Transformations in Materials*, edited by R. W. Cahn, P. Haasen, and E. J. Kramer (VCH, Weinheim, 1991), Vol. 5 of *Materials Science and Technology*, p. 339.
[44] H. Czichos, *Adolf Martens and the Research on Martensite* (E. Hornbogen und N. Jost, Oberursel, 1989), Chap. 1, p. 3.
[45] Martensitic transformations are typical for Fe and its alloys. A common crystallographic orientational relationship between the parent and the product phase is the Nishyama-Wassermann: $(111)_{\mathrm{fcc}}\parallel(101)_{\mathrm{bcc}}$, $[1\bar{2}1]_{\mathrm{fcc}}\parallel[10\bar{1}]_{\mathrm{bcc}}$ or equivalently: $(111)_{\mathrm{fcc}}\parallel(110)_{\mathrm{bcc}}$, $[1\bar{1}0]_{\mathrm{fcc}}\parallel[001]_{\mathrm{bcc}}$.
[46] K. Kadau, R. Meyer, and P. Entel, Surf. Rev. Lett. **6**, 35 (1999).
[47] D. Hayes, J. Appl. Phys. **45**, 1208 (1974).
[48] M. Knudson and Y. Gupta, J. Appl. Phys. **91**, 9561 (2002).
[49] K. Kadau, T. C. Germann, P. S. Lomdahl, and B. L. Holian, AIP Conf. Proc. **620**, 351 (2002).
[50] Y. B. Zel'dovich and Y. P. Raizer, *Physics of Shock Waves and High-Temperature Hydrodynamic Phenomena* (Academic, New York, 1967).
[51] L. Veeser, G. T. Gray, III, J. Vorthman, P. Rodriguez, R. Hixson, and D. Hayes, AIP Conf. Proc. **505**, 73 (2000).
[52] J. C. Boettger and D. C. Wallace, Phys. Rev. B **55**, 2840 (1997).
[53] The shock velocity in the limit of $u_p \rightarrow 0$ is equal to the sound velocity c and depends on the crystallographic shock direction: $\rho c^2_{[001]}=C_{11}$, $\rho c^2_{[011]}=(C_{11}+C_{12}+2C_{44})/2$, $\rho c^2_{[111]}=(C_{11}+2C_{12}+4C_{44})/3$, where C_{11}, C_{12}, C_{44} are the elastic constants of the cubic crystal and ρ is the density.

[54] J. Schiøtz, F. D. D. Tolla, and K. W. Jacobsen, Nature (London) **391**, 561 (1998).

[55] R. Ravelo, B. L. Holian, T. C. Germann, and P. S. Lomdahl, Phys. Rev. B **70**, 014103 (2004).

[56] T. Germann, unpublished work.

[57] C. S. Yoo, N. C. Holmes, M. Ross, D. J. Webb, and C. Pike, Phys. Rev. Lett. **70**, 3931 (1993).

[58] J. M. Brown and R. G. McQueen, J. Geophys. Res. **91**, 7485 (1986).

[59] Q. Williams, R. Jeanloz, J. Bass, B. Svendsen, and T. Ahrens, Science **236**, 181 (1987).

[60] T. Ahrens, K. G. Holland, and G. Chen, Geophys. Res. Lett. **29**, 54 (2002).

[61] J. H. Nguyen and N. Holmes, Nature (London) **427**, 339 (2004).

[62] We calculated the thermodynamic melting curve in a series of two-phase simulations in the NVE ensemble: a sample was filled half with liquid and half with perfect solid fcc, the liquid (solid) portion increased if the temperature was initially too high (low) until a pressure and temperature on the melting curve was reached. The advantage of this method over a two-phase simulation in the NPT ensemble is that one gets a point on the melting curve for each run rather than doing a series of runs to bracket a (well defined) point on the melting curve. However, one has to check if the final mixed state is hydrostatic; if this is not the case the initial compression or temperature has to be changed until the final state is hydrostatic.

[63] A. Belonoshko and R. Ahuja, Phys. Earth Planet. Inter. **102**, 171 (1997).

[64] B. L. Holian, H. Flaschka, and D. W. McLaughlin, Phys. Rev. A **24**, 2595 (1981).

[65] V. Nesterenko, AIP Conf. Proc. **505**, 177 (2000).

[66] K. Kadau, unpublished work.

[67] J. Roth (private communication).

[68] D. H. Kalantar, J. F. Belak, G. W. Collins, J. D. Colvin, H. M. Davies, J. H. Eggert, T. C. Germann, J. Hawreliak, B. L. Holian, K. Kadau, P. S. Lomdahl, H. E. Lorenzana, M. A. Meyers, K. Rosolankova, M. S. Schneider, J. Sheppard, J. S. Stölken, and J. S. Wark, Phys. Rev. Lett. **95**, 075502 (2005).

[69] B. Yaakobi, T. R. Boehly, D. D. Meyerhofer, T.J.B. Collins, B. A. Remington, P. G. Allen, S. M. Pollaine, H. E. Lorenzana, and J. H. Eggert, Phys. Rev. Lett. **95**, 075501 (2005).

[70] R. Ravelo and M. Baskes, Phys. Rev. Lett. **79**, 2482 (1997).

[71] M. I. Mendelev, S. Han, D. J. Srolovitz, G. J. Ackland, D. Y. Sun, and M. Asta, Philos. Mag. **83**, 3977 (2003).